Monthly Notices of the ROYAL ASTRONOMICAL SOCIETY

MNRAS **544,** 855–865 (2025) https://doi.org/10.1093/mnras/staf1738
Advance Access publication 2025 October 13

Characterization of the chemical evolution of CH_4 ices under processing by cosmic ray analogues with the PROCODA code – I. Effective reaction rate coefficients and chemical equilibrium phase

S. Gerasimenko,[1] G. A. Carvalho ,[1,2]★ F. Zanatto,[3] F. K. Santana[3] and S. Pilling[4]

[1]*Departamento de Física, Universidade Tecnológica Federal do Paraná, Medianeira 85884-000, PR, Brazil*
[2]*Programa de Pós-Graduação em Física e Astronomia, Universidade Tecnológica Federal do Paraná, Jardim das Americas, Curitiba 82590-300, PR, Brazil*
[3]*Departamento de Física, Universidade Tecnológica Federal do Paraná, Curitiba 81280-340, PR, Brazil*
[4]*Instituto de Pesquisa e Desenvolvimento, Universidade do Vale do Paraíba, São José dos Campos 12244-000, SP, Brazil*

Accepted 2025 September 12. Received 2025 August 19; in original form 2025 April 15

ABSTRACT

Methane (CH_4), the simplest alkane, is a fundamental component of astrophysical ices, particularly in the outer Solar system and the interstellar medium. Understanding its chemical evolution under energetic particle irradiation is essential for modelling these environments. In this work, we investigate the chemical evolution of pure methane ice subjected to high-energy ion irradiation until chemical equilibrium is reached. We employ the PROCODA code to simulate the time-dependent evolution of molecular abundances and to determine effective reaction rate coefficients. The simulations are constrained using experimental data from a previous study, in which pure CH_4 ice at 16 K was irradiated, providing the necessary input parameters for the model. Our reaction network comprises 1857 chemical reactions involving 36 molecular species, both observed and unobserved by Fourier-transform infrared spectroscopy during the experiment. The best-fitting model satisfies multiple criteria: a low χ^2 for observed species, a desorption yield consistent with experimental estimates, similar trends in abundance evolution for observed and unobserved species, and overall mass conservation. At chemical equilibrium, the most abundant species predicted by the model are H_2 (38.0 per cent), CH_4 (20.8 per cent), H (17.0 per cent), and $CH_3CH_2CH_3$ (16.9 per cent). The total desorption yield is calculated as 5.4×10^4 molecules/ion, and the effective destruction cross-section of CH_4 is 7.1×10^{-13} cm^2. The reaction rate coefficients and equilibrium abundances derived from this study provide valuable inputs for astrochemical models, enhancing our understanding of CH_4 processing in interstellar ices under cosmic ray irradiation.

Key words: molecular processes – software: simulations – astrometry – ISM: abundances.

1 INTRODUCTION

Astrophysical ices are continually exposed to energetic processes in space, including bombardment by cosmic rays (CRs) and irradiation by high-energy photons such as ultraviolet (UV) and X-rays. These interactions play a crucial role in driving the chemistry of molecular ices in cold environments like dense molecular clouds and icy planetary surfaces. CRs, comprising protons, electrons, and heavy ions, are produced by various astrophysical phenomena, while low-energy CRs are generally associated with solar wind particles. The origin of high-energy CRs remains an open and active area of research (T. K. Gaisser, R. Engel & E. Resconi 2016), even though they were first detected over six decades ago (J. Linsley, L. Scarsi & B. Rossi 1961; J. Linsley 1963). Current evidence suggests that such particles may originate from supernova remnants or extragalactic sources (A. Aab & others 2017).

A key threshold in CR classification lies near 5×10^{17} eV, marking the transition from Galactic to extragalactic origins, according to A. Aab et al. (2017). Particles with energies above this threshold are referred to as ultra-high-energy cosmic rays. As these CRs propagate through the interstellar medium (ISM), they interact with icy grains, triggering molecular dissociation and initiating complex chemical networks (W. J. Maciel 2013; J. P. Williams 2021). Such processes are believed to contribute significantly to the synthesis of prebiotic molecules in space.

Among the molecular constituents of astrophysical ices, methane (CH_4) stands out as a key compound. As the simplest alkane, methane is not only abundant in the outer Solar system; detected on Pluto (G. R. Gladstone et al. 2016; A. Poro et al. 2021), Triton (J. L. Elliot et al. 2000; K. Ohno et al. 2021; B. Sicardy et al. 2024), Eris, and Makemake (C. Dumas et al. 2007; C. R. Glein et al. 2024); but also in the ISM itself (J. H. Lacy et al. 1991). Observations have recently expanded to include detections of methane in the Martian atmosphere (V. Formisano et al. 2004), in the atmosphere of an exoplanet about 163 light-years away via the *James Webb Space Telescope* (*JWST*)

★ E-mail: gacarvalho@utfpr.edu.br

(T. J. Bell et al. 2023), and in strong emission from the cool brown dwarf CWISEP J193518.59-154620.3, also observed by *JWST* (J. K. Faherty et al. 2024).

Despite its relative chemical stability due to strong sigma bonds, methane can undergo significant transformation under CR irradiation. Energetic particles can deposit sufficient energy to break these bonds, producing reactive species such as methyl radicals (CH_3), atomic hydrogen (H), and various secondary products. These reactions are central to the formation of more complex organic molecules and make CH_4 a particularly informative target in laboratory simulations of astrophysical ice chemistry.

A number of experimental studies have investigated the irradiation of pure and mixed methane ices with different types of ions (S. Pilling et al. 2010; A. L. F. de Barros et al. 2011; Ph. Boduch et al. 2012; X. Y. Lv et al. 2012; C. F. Mejía et al. 2013; P. Boduch et al. 2015; F. A. Vasconcelos et al. 2017). These experiments have consistently highlighted the critical role of CH_4 in astrochemical evolution, especially in the synthesis of complex organic compounds (S. Pilling et al. 2009; F. A. de Vasconcelos et al. 2017, 2020; D. V. Mifsud et al. 2023; K. A. Kipfer et al. 2024). Understanding how methane behaves under various irradiation and temperature conditions is therefore essential for building accurate astrochemical models.

To simulate these chemical processes, we employ the PROCODA code, initially developed by S. Pilling, G. A. Carvalho & W. R. M. Rocha (2022) to model the irradiation of pure CO_2 ices with CR analogues (e.g. 52 MeV Ni ions at 13 K) and UV photons (10 eV at 8 K; R. Martín-Doménech et al. 2015). The code relies on a defined network of chemical reactions and desorption mechanisms to simulate the time-dependent chemical evolution of irradiated ices. Since its introduction, PROCODA has been successfully applied to the study of acetonitrile ice irradiated with soft X-rays (G. A. Carvalho, S. Pilling & B. R. L. Galvão 2022; G. A. Carvalho, S. Pilling & S. Gerasimenko 2024) and has been upgraded to incorporate thermochemistry-informed ordering of effective reaction rate coefficients (ERCs; S. Pilling et al. 2023a). This upgrade has enabled improved modelling of CO_2 ice under ion, UV, and electron irradiation, and was recently employed in the analysis of CO-enriched ices at multiple temperatures (S. Pilling et al. 2024).

In the present study, we apply the upgraded version of PROCODA to simulate the chemical evolution of pure CH_4 ices subjected to CR analogue irradiation. Our focus is on determining effective reaction rate coefficients and the chemical equilibrium abundances that emerge from the simulations. Future studies will examine the dominant chemical formation and destruction pathways of certain species, their evolution with increasing fluence and the irradiation-induced desorption. The astrophysical relevance of these processes will also be assessed.

The experimental data and computational procedures are detailed in Section 2. The main simulation results are presented and analysed in Section 3, followed by a discussion of their astrophysical significance in Section 4. Final remarks and conclusions are summarized in Section 5.

2 METHODOLOGY

2.1 Experimental data set

The experimental data used in this study were obtained in a previous work by F. A. Vasconcelos et al. (2017), in which methane (CH_4) ices were irradiated with energetic ions. The experiments were conducted at the Grand Accélérateur National d'Ions Lourds (GANIL) in Caen, France, utilizing the high-vacuum chamber CASIMIR (Chambre d'Analyse par Spectroscopie Infrarouge des Molécules IRradiées) and the IRRSUD (IR Radiation SUD) beamline.

An infrared (IR) spectrum of the pristine sample was collected prior to irradiation. The sample was then bombarded with 15.7 MeV $^{16}O^{5+}$ ions at a flux of 9×10^9 ions$\cdot$ cm$^{-2}\cdot$ s^{-1}, reaching a maximum fluence of 1.1×10^{14} ions$\cdot$ cm^{-2}. *In situ* Fourier-transform infrared (FTIR) spectroscopy was employed throughout the irradiation to monitor chemical changes in the ice. The density of the CH_4 ice was assumed to be 0.44 g$\cdot$ cm^{-3}, corresponding to an initial column density of 9.7×10^{19} molecules$\cdot$ cm^{-2}. These experimental results were used as input parameters for the numerical modelling performed using the PROCODA code.

2.2 The PROCODA modelling approach

The PROCODA code, originally introduced in S. Pilling et al. (2022), solves a system of coupled differential equations to simulate the chemical evolution of irradiated ices. The change in column density N_i of each species i over time is given by:

$$\frac{dN_i}{dt} = -\mathrm{DES}_i(t) - \sum_{d1} k_{d1} N_i(t) - \sum_{d2} \frac{k_{d2} N_i(t) N_a(t)}{L} + \sum_{p1} k_{p1} N_a(t) + \sum_{p2} \frac{k_{p2} N_a(t) N_b(t)}{L}, \quad (1)$$

where:

(i) $N_i(t)$ is the column density of species i [molecules$\cdot$ cm^{-2}],
(ii) k_{p1} and k_{p2} are production rate coefficients (unimolecular and bimolecular),
(iii) k_{d1} and k_{d2} are destruction rate coefficients,
(iv) N_a and N_b are the column densities of reactant species a and b,
(v) L is the average sample thickness (cm),
(vi) $\mathrm{DES}_i(t) = k_{\mathrm{des},i}\,\Omega_i(t) N_i(t)$ represents the desorption term, dependent on the intrinsic desorption rate $k_{\mathrm{des},i}$ (s^{-1}) and the surface coverage $\Omega_i(t)$ (dimensionless, between 0 and 1).

The chemical network employed in this study includes 1857 reactions involving 36 molecular species. Of these, seven were experimentally observed (CH_4, CH_3, CHCH, C_2H_4, CH_3CH_3, $CH_3CH_2CH_3$, and $CH_2CHCH_2CH_3$), while the remaining 29 are plausible intermediate or final products inferred from reaction pathways (e.g. H, H_2, CH, C_2 species, and larger hydrocarbons). The full list of reactions and species is available in the supplementary material. Fig. 1 provides the structural representations of all species considered.

2.2.1 *Score function and optimization*

To calibrate the model and assess its agreement with experimental data, a score function (SF) was defined to guide the minimization algorithm. This function aggregates weighted residuals between observed and modelled column densities for all seven detected

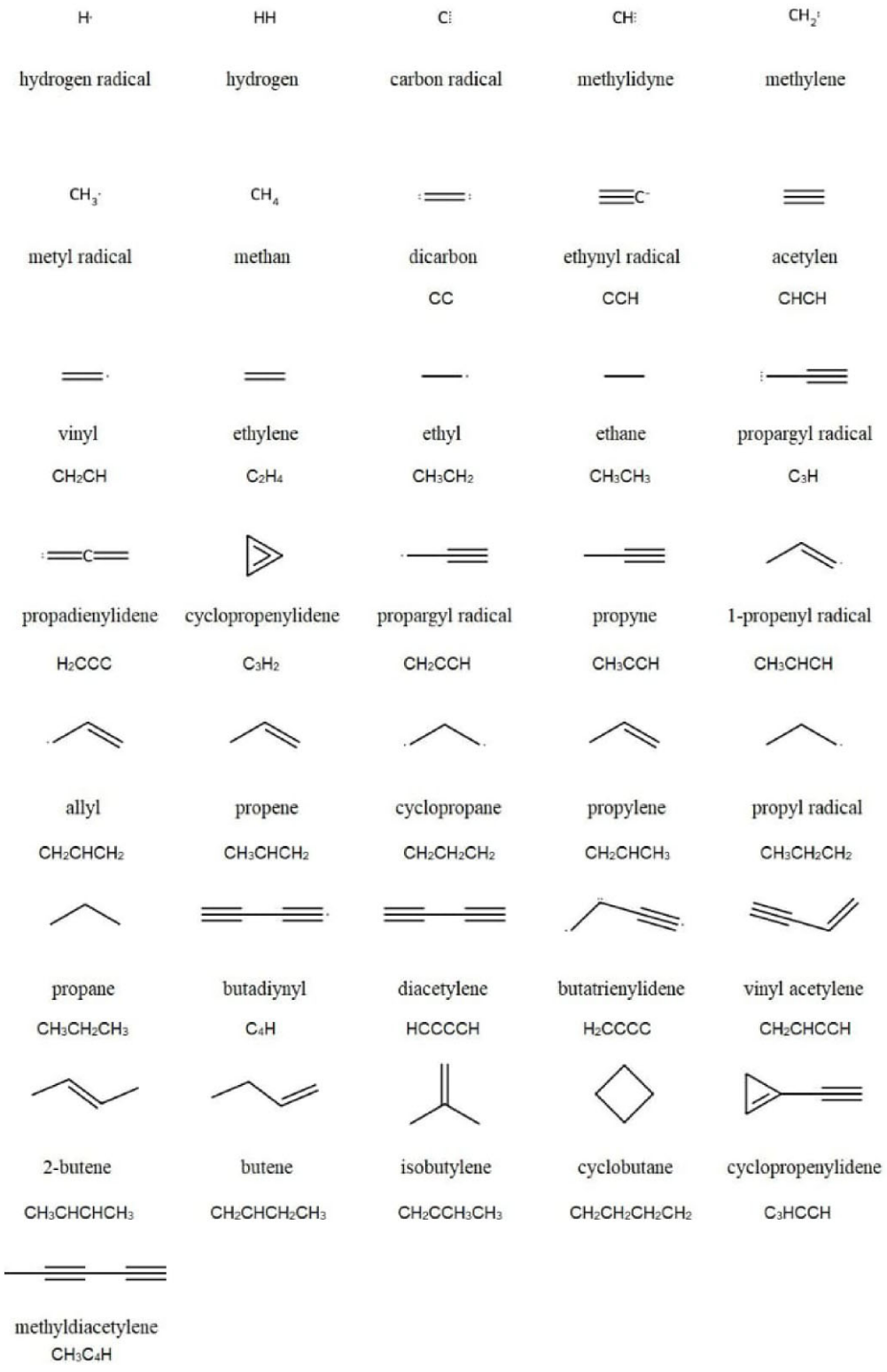

Figure 1. The names and structure of the molecular species considered for the chemical reaction network.

species:

$$\begin{aligned}
\mathrm{SF} = {} & p1 \times \sum \frac{(\mathrm{oCH4_{data}} - \mathrm{oCH4_{model}})^2}{\mathrm{oCH4_{data}}} \\
& + p2 \times \sum \frac{(\mathrm{oCH3_{data}} - \mathrm{oCH3_{model}})^2}{\mathrm{oCH3_{data}}} \\
& + p3 \times \sum \frac{(\mathrm{oCHCH_{data}} - \mathrm{oCHCH_{model}})^2}{\mathrm{oCHCH_{data}}} \\
& + p4 \times \sum \frac{(\mathrm{oC2H4_{data}} - \mathrm{oC2H4_{model}})^2}{\mathrm{oC2H4_{data}}} \\
& + p5 \times \sum \frac{(\mathrm{oCH3CH3_{data}} - \mathrm{oCH3CH3_{model}})^2}{\mathrm{oCH3CH3_{data}}} \\
& + p6 \times \sum \frac{(\mathrm{oCH3CH2CH3_{data}} - \mathrm{oCH3CH2CH3_{model}})^2}{\mathrm{oCH3CH2CH3_{data}}} \\
& + p7 \times \sum \frac{(\mathrm{oCH2CHCH2CH3_{data}} - \mathrm{oCH2CHCH2CH3_{model}})^2}{\mathrm{oCH2CHCH2CH3_{data}}} \\
& + p8 \times [(1 - \mathrm{MSC}_f) + (1 - \mathrm{MSOo}_f) + (1 - \mathrm{MSCo}_m)] \\
& + p9 \times (1 - \mathrm{DSC}) + p10 \times (1 - \mathrm{SSC}), \qquad (2)
\end{aligned}$$

where:

(i) $\mathrm{oX_{data}}$ and $\mathrm{oX_{model}}$ are the experimental and modelled values for species X,

(ii) MSC_f = mass similarity criterion (at the end of simulation),

(iii) MSOo_f and MSCo_m = column mass similarity criteria for observed species at the end and at the middle of simulation,

(iv) DSC = desorption similarity criterion (from comparison with desorption data in F. A. Vasconcelos et al. 2017),

(v) SSC = slope similarity criterion at large fluences,

(vi) p_1 through p_{10} are dimensionless weights applied to each term.

The SF thereby integrates both quantitative deviations and qualitative trends (e.g. slope behaviour, mass conservation, and desorption yield) into the fitting routine. The effective reaction rate coefficients (k_{values}) of the chemical reactions are iteratively optimized to minimize SF. A detailed explanation of the optimization and modelling strategy can be found in S. Pilling et al. (2022, 2023a, c).

3 RESULTS

The evolution of the column densities with time, the molecular abundances at chemical equilibrium, and the reaction rate coefficients obtained in the best-fitting model are given in the following sections.

3.1 Column density evolution and effective reaction rate coefficients

The best-fitting model that satisfies the imposed constraint (smallest SF), for the irradiation of CH_4 ice with medium-mass ions (15.7 MeV $^{16}O^{5+}$) is shown in Fig. 2. In particular, panel (a) of Fig. 2 displays the column densities of all 36 species considered in the model, while panel (b) highlights only the observed species. Experimental data points are represented by geometric markers. It is worth to recall here that the experimental data and assignments were performed in (F. A. Vasconcelos et al. 2017). The plot title summarizes the modelling constraints: Mass Similarity Criterion (MSC) of approximately 97 per cent, Slope Similarity Criterion (SSC) near 100 per cent, total desorption yield of 4.65×10^4 molecules/ion, total χ^2 for observed species of about 27, and an SF of ∼245.

The experimental desorption yield was measured to be 7.3×10^5 molecules per ion impact (F. A. Vasconcelos et al. 2017), which is an order of magnitude higher than predicted by the model. This discrepancy suggests that the real desorption process is more efficient than the model currently accounts for, possibly due to additional physical mechanisms not included in the present simulation.

A significant discrepancy is observed for the $CH_2CHCH_2CH_3$ molecule, whose modelled column density differs from the experimental estimate by nearly two orders of magnitude. This inconsistency likely arises from the difficulty in confidently assigning IR spectral features to this molecule. The identification was based on a single absorption band at 913 $\mathrm{cm^{-1}}$, which may also be attributed to butene, as previously suggested in the literature (Y. S. Kim et al. 2010; F. A. Vasconcelos et al. 2017), following irradiation of C_2H_6 ice at 10 K. Relying on a single IR feature for molecular identification is inherently uncertain; thus, we argue that the experimental assignment of $CH_2CHCH_2CH_3$ made by authors of (F. A. Vasconcelos et al. 2017) is likely inaccurate and should be reconsidered in light of the model results. Further supporting this conclusion is the fact that the inferred abundance of $CH_2CHCH_2CH_3$, a four-carbon chain, exceeds that of simpler species such as CH_3, which is chemically implausible. This also casts doubt on the experimental estimates for $CH_3CH_2CH_3$, whose abundance may be similarly overestimated.

From Fig. 2, it is clear that the ice approaches chemical equilibrium after approximately 6000 s of irradiation. This behaviour is reflected in both the experimental data and model predictions. The SSC confirms that the trends of column density evolution for observed and unobserved species are alike, primarily due to the ongoing desorption processes.

Based on the best-fitting model, we determined the effective reaction rate coefficients (ERCs) for the 1857 reactions considered. Detailed values, along with branching ratios within reaction groups and additional metadata, are provided in the supplementary material.

We also calculated the average effective reaction rate coefficients for direct dissociation processes (first-order reactions initiated by ion impact, excluding desorption) and bimolecular reactions. The average rate coefficient and corresponding dissociation cross-section for direct dissociations are:

$$\begin{aligned}
\bar{k}_d &= 6.42 \times 10^{-3}\ \mathrm{s^{-1}}, \\
\bar{\sigma}_d &= \frac{\bar{k}_d}{\phi_i} = 7.1 \times 10^{-13}\ \mathrm{ions \cdot cm^{-2} \cdot s^{-1}}, \qquad (3)
\end{aligned}$$

where ϕ_i is the ion flux employed in the experiment ($\phi_i = 9 \times 10^9$ ions $\cdot$ $\mathrm{cm^{-2}} \cdot \mathrm{s^{-1}}$).

The average value of the effective reaction rate coefficients of bimolecular reactions (typical two-body collision) is:

$$\bar{k}_{A+B} = 7.02 \times 10^{-25}\ \mathrm{cm^3 \cdot molecule^{-1} \cdot s^{-1}}. \qquad (4)$$

Table 1 presents a comparison between the effective dissociation cross-section for methane ice obtained in this work and values reported in the literature. The average value derived from our model ($\bar{\sigma}_d = 7.1 \times 10^{-13}\ \mathrm{cm^2}$) is approximately one order of magnitude higher than the experimental result reported by F. A. Vasconcelos et al. (2017) ($2.32 \pm 0.46 \times 10^{-14}\ \mathrm{cm^2}$). Moreover, it exceeds by nearly two orders of magnitude the cross-sections reported for CH_4 irradiated with $^{16}O^{7+}$ ions in previous studies (A. L. F. de Barros et al. 2011; C. F. Mejía et al. 2013).

3.2 Dissociation processes (for observed species)

In this section, we briefly consider the dissociation reactions of the observed species. The PROCODA code gives the branching ratio (BR in percentage) of direct radiation-induced reactions, as detailed in the following.

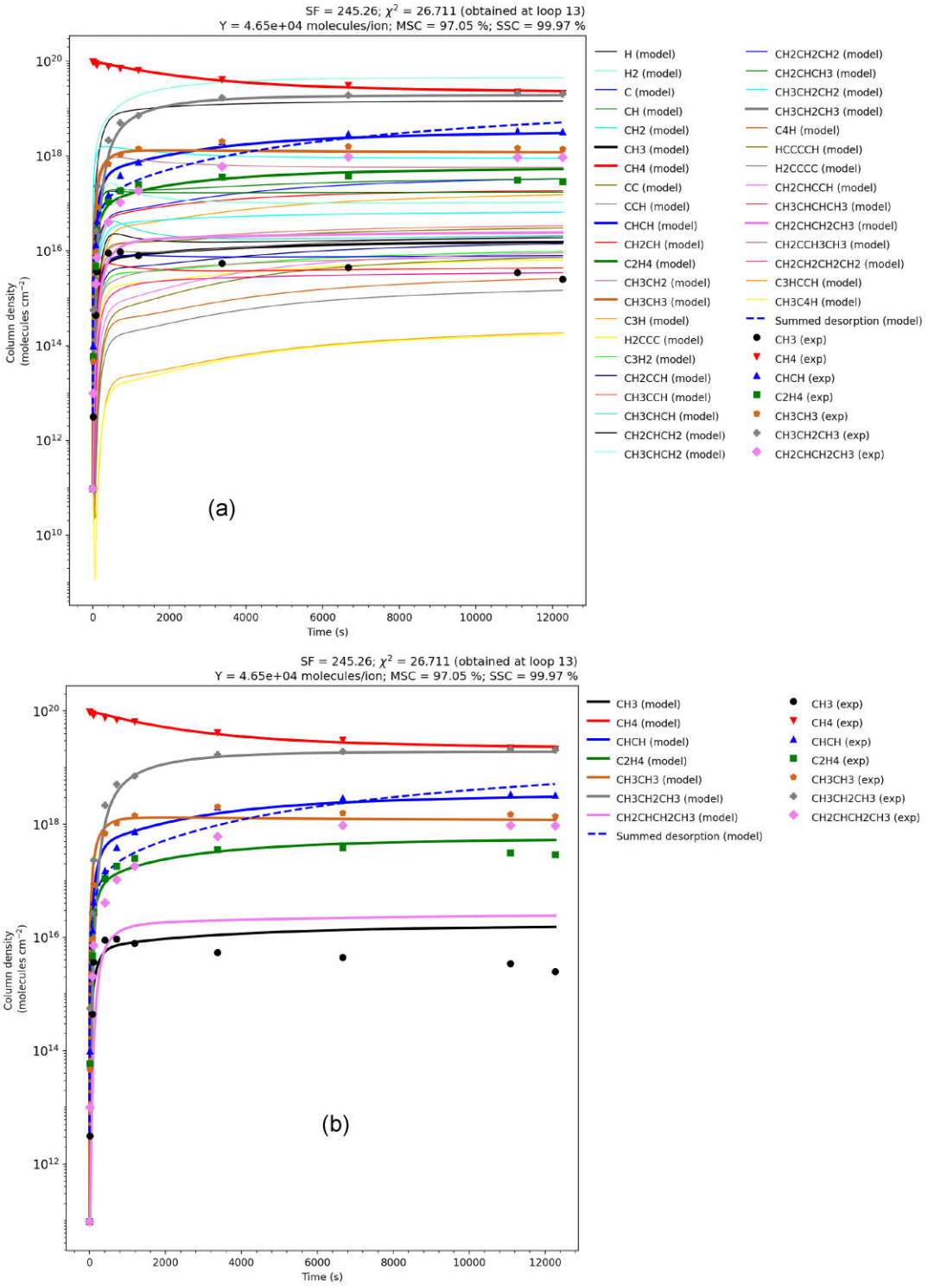

Figure 2. Column density evolution with time for irradiation of pure methane ice at 16 K with 15.7 MeV $^{16}O^{5+}$. Panel (a) shows the model curves for all species together with the experimental data of observed species, whereas panel (b) shows the experimental data and model curves for the observed species only.

3.2.1 CH_4 (parent species)

The chemical reaction network involves only two reactions of direct dissociation of CH_4, one leading to the formation of the CH_3 radical and H atom and the other to CH_2 and H_2.

$$CH_4 \rightarrow CH_3 + H, \quad k_{11} = 4.3 \times 10^{-7}\ s^{-1} \ (BR = 0.25\ \%), \tag{5}$$

$$CH_4 \rightarrow CH_2 + H_2, \quad k_{67} = 1.7 \times 10^{-4}\ s^{-1} \ (BR = 99.75\ \%). \tag{6}$$

At this stage, the formation of the methylidyne radical (CH) cannot be directly attributed to the dissociation of CH_4, since the chemical reaction network does not include reactions involving more than two reactants or products. Nevertheless, the formation of CH has

Table 1. Comparison of the effective destruction cross-section of CH_4 obtained in this work with literature values using energetic ions as the radiation source.

Projective	Sample, experiment or model	$\bar{\sigma}_d$ (cm^2)	References
15.7 MeV $^{16}O^{5+}$	Pure CH_4 ice, experiment	$2.32 \pm 0.46 \times 10^{-14}$	(F. A. Vasconcelos et al. 2017)
15.7 MeV $^{16}O^{5+}$	Pure CH_4 ice, model	7.1×10^{-13} (first-order reactions)	This work
220 MeV $^{16}O^{7+}$	Pure CH_4 ice, experiment	3.8×10^{-15}	(A. L. F. de Barros et al. 2011)
220 MeV $^{16}O^{7+}$	Pure CH_4 ice, experiment	4×10^{-15}	(C. F. Mejía et al. 2013)

been experimentally observed by F. A. Vasconcelos et al. (2017), suggesting that it may result from subsequent secondary reactions. According to the branching ratios of the selected reactions, the most favourable dissociation channel for CH_4 is the formation of CH_2 and H_2, as indicated by the high branching ratio shown in equation (6).

3.2.2 C_2H_2 (acetylene molecule)

The radiation induced dissociation reactions of C_2H_2 considered in the model are the following:

$$C_2H_2 \rightarrow H + CCH, \quad k_{15} = 2.1 \times 10^{-5}\ s^{-1} \ (BR = 0.6\ \%), \tag{7}$$

$$C_2H_2 \rightarrow H_2 + CC, \quad k_{69} = 7.4 \times 10^{-4}\ s^{-1} \ (BR = 22.0\ \%), \tag{8}$$

$$C_2H_2 \rightarrow C + CH_2, \quad k_{112} = 1.4 \times 10^{-3}\ s^{-1} \ (BR = 41.5\ \%), \tag{9}$$

$$C_2H_2 \rightarrow CH + CH, \quad k_{164} = 1.2 \times 10^{-3}\ s^{-1} \ (BR = 35.9\ \%). \tag{10}$$

It can be seen that the acetylene molecule is most likely to dissociate into two methylidyne (CH) radicals, or, with nearly equivalent probability, into C and CH_2; pathways that were not predicted by F. A. Vasconcelos et al. (2017). Although less probable, the formation of H_2 and a CC fragment is also expected to occur to a non-negligible extent.

3.2.3 C_2H_4 (ethylene)

The direct dissociation of the ethylene molecule (C_2H_4) primarily occurs through two main chemical reactions, as listed below:

$$C_2H_4 \rightarrow H + CH_2CH, \quad k_{19} = 6.6 \times 10^{-2}\ s^{-1} \ (BR = 91.6\ \%), \tag{11}$$

$$C_2H_4 \rightarrow H_2 + C_2H_2, \quad k_{73} = 4.5 \times 10^{-3}\ s^{-1} \ (BR = 6.3\ \%). \tag{12}$$

The dissociation of the ethylene molecule (C_2H_4) is most likely to proceed via the formation of H atoms and the C_2H_3 radical. The production of H_2 and C_2H_2 is also possible, though less favoured. According to computational calculations, the remaining dissociation pathways have negligible contribution.

3.2.4 C_2H_6 (ethane)

The three most important chemical reactions for the dissociation of the C_2H_6 molecule are:

$$C_2H_6 \rightarrow H + CH_3CH_2, \quad k_{23} = 6.7 \times 10^{-4}\ s^{-1} \ (BR = 32.2\ \%), \tag{13}$$

$$C_2H_6 \rightarrow H_2 + C_2H_4, \quad k_{77} = 1.8 \times 10^{-4} s^{-1} \ (BR = 8.8\ \%), \tag{14}$$

$$C_2H_6 \rightarrow CH_2 + CH_4, \quad k_{214} = 1.2 \times 10^{-3}\ s^{-1} \ (BR = 59.0\ \%). \tag{15}$$

The reaction (15) has the largest BR indicating that C_2H_6 provides some returning to the father molecule methane, this is accordance results presented in (F. A. Vasconcelos et al. 2017).

3.2.5 C_3H_8 (propane)

The relevant chemical reactions for the dissociation of the C_3H_8 molecule are only two, besides the chemical reaction network includes seven:

$$C_3H_8 \rightarrow CH_2 + CH_3CH_3, \quad k_{236} = 4.6 \times 10^{-5}\ s^{-1} \ (BR = 7.5\ \%), \tag{16}$$

$$C_3H_8 \rightarrow CH_4 + C_2H_4, \quad k_{315} = 5.5 \times 10^{-4}\ s^{-1} \ (BR = 91.5\ \%). \tag{17}$$

The most important chemical reaction leads to the formation of CH_4 and C_2H_4, while the other results in the formation of CH_2 and C_2H_6. Virtually, the dissociation of propane may be directly related to the formation of these four species.

3.3 C_4H_8 (isobutylene)

The chemical reaction network includes 11 chemical reactions for the dissociation of C_4H_8, of which four are dominant, while the others are either nearly negligible or entirely insignificant, as shown below.

$$C_4H_8 \rightarrow CH + CH_3CH_2CH_2, \quad k_{204} = 5.6 \times 10^{-3}\ s^{-1} \ (BR = 11.1\ \%), \tag{18}$$

$$C_4H_8 \rightarrow CH_2 + CH_2CH_2CH_2, \quad k_{254} = 6.3 \times 10^{-3}\ s^{-1} \ (BR = 12.4\ \%), \tag{19}$$

$$C_4H_8 \rightarrow CH_4 + CH_3CCH, \quad k_{318} = 2.9 \times 10^{-2}\ s^{-1} \ (BR = 56.9\ \%), \tag{20}$$

$$C_4H_8 \rightarrow C + CH_3CH_2CH_3, \quad k_{154} = 6.8 \times 10^{-3}\ s^{-1} \ (BR = 13.3\ \%). \tag{21}$$

Fig. 3 summarizes the possible reaction pathways leading to the formation of the observed species based on their dissociation reactions. All reactions associated with the formation or destruction of a given species can be derived from the simulations; however, a more detailed analysis will be presented in a forthcoming publication related to some of the considered species.

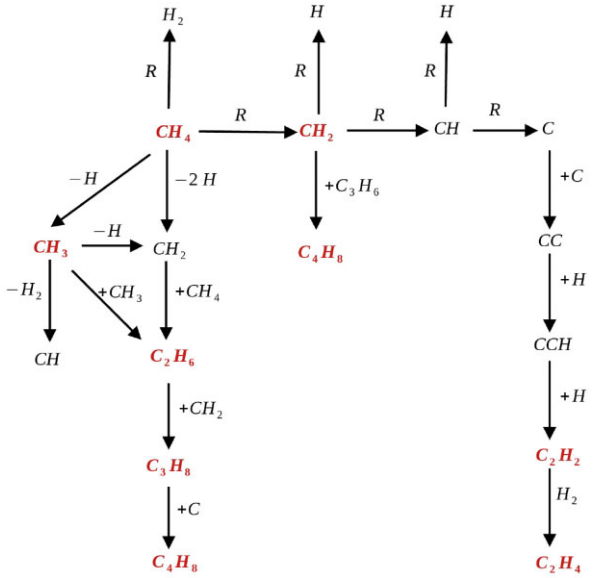

Figure 3. Reaction pathways for the formation of observed species based on their direct dissociation reactions during the irradiation of the methane ice with CR analogues.

3.4 Chemical equilibrium phase

The reduction in molecular abundance changes with increasing irradiation time indicates the approach to chemical equilibrium (CE) within the sample. The CE phase is the stage where the variation in total summed chemical abundances becomes negligible, less than 1 per cent of the overall abundance (S. Pilling et al. 2022). Based on the data from F. A. Vasconcelos et al. (2017), CE is reached at a fluence of 9×10^9 cm$^{-2}\cdot$ s^{-1}. Fig. 4 displays the molecular abundances expressed as percentages at the CE phase, commonly referred to as the equilibrium branching ratio (EBR per cent).

In Fig. 4, observed species are highlighted in blue, while non-observed species are shown in red. The PROCODA computational methodology uniquely enables the quantification and characterization of these non-observable species. Table 2 provides a comprehensive list of molecular abundances at chemical equilibrium.

At chemical equilibrium, the species H, H_2, CH_4, and $CH_3CH_2CH_3$ constitute the majority of the molecular abundance in the sample, accounting for approximately 93 per cent in total. The species H and H_2 were not detected experimentally: atomic hydrogen is IR-inactive, while molecular hydrogen's characteristic IR band around 2800 cm^{-1} overlaps with features used to identify C_2H_6. Twelve other species: CH_3CH_3, CHCH, CH_2, CH_2CHCH_3, CH_2CH, CH_3CH_2, C_2H_4, C, CH, C_3H, CH_3CH_2, and CH_3CHCH_2 have molecular abundances ranging from 0.1 per cent to 2.75 per cent, whereas the remaining species have abundances below 0.045 per cent, rendering them essentially negligible.

Despite their low abundances, molecules such as propadienylidene (H_2CCC, EBR = 0.006 per cent) and vinyl acetylene (CH_2CHCCH, EBR = 0.008 per cent) may still play important roles in organic synthesis and serve as building blocks for more complex compounds. However, according to the simulation these species are not expected to be abundant in CH_4-dominated ices. Moreover, molecules like vinyl acetylene have yet to be detected in space (EBR = 0.003 per cent). Notably, the total molecular abundance of observed species is roughly 15 per cent lower than that of non-observed species, highlighting the need for improvements in experimental detection methods for providing more information on the sample composition.

3.5 Comparison with previous calculations and other methodology

Table 3 presents the average values of the ERCs, desorption rate, and desorption yield obtained from the best-fitting model developed in this work. These results are compared with average values previously reported for pure CH_4, CO, CO_2, H_2O, and CH_3CN ices, derived using a similar methodology. All ice samples were irradiated under varying temperatures and by different radiation sources. As shown by C. H. da Silveira & S. Pilling (2024), the ERC values for H_2O ice are strongly influenced by both temperature and the type of radiation. The highest ERC was observed for X-ray irradiation at 12 K, whereas a significantly lower ERC was reported for Ni ion irradiation at 13 K.

A comparison between the irradiation of pure CO_2 and pure H_2O ices under identical conditions (13 K, 52 MeV Ni ions) reveals a significantly lower ERC value for H_2O (3.2×10^{-6} s^{-1}) compared to CO_2 (2.9×10^{-3} s^{-1}). This highlights the strong dependence of the ERC on the chemical composition of the sample, even under the same irradiation energy and temperature. Furthermore, when comparing the ERC values of pure CH_4 irradiated with $^{16}O^{5+}$ ions to those of CO and CO_2 ices irradiated with heavier Ni ions, it becomes evident that Ni ion irradiation leads to significantly higher ERCs for both CO and CO_2 ices.

The lowest ERC value was obtained for acetonitrile (CH_3CN) ice irradiated by X-rays at 13 K, yielding 6.2×10^{-6} s^{-1}. As shown in Table 3, this value is lower than that for pure H_2O ice irradiated under similar conditions (12 K, X-rays), indicating that X-ray irradiation is less effective for acetonitrile ice in this temperature range.

Table 3 also provides ERC values for both radiation-induced direct dissociation reactions and bimolecular reactions. As suggested by S. Pilling et al. (2023c), the average ERC for CO ice is higher than that for CO_2 ice, which may be attributed to the greater mobility and diffusion of CO molecules within the ice matrix during irradiation. In contrast, the average ERC for CH_3CN ice is lower than that for CO_2 ice, suggesting reduced reactivity or lower molecular mobility under the same conditions.

Additionally, as noted by S. Pilling et al. (2023c), the ERCs for radiation-induced direct reactions account not only for excitation processes triggered by the incoming radiation but also for the effects of secondary electron collisions within the ice, which can lead to product formation. The same consideration is applied in the calculation of ERCs for bimolecular reactions.

Interestingly, the ERCs for bimolecular reactions of pure H_2O and pure CO ices irradiated by Ni ions are nearly identical: 4.3×10^{-24} and 4.4×10^{-24} cm^3, respectively. Likewise, the ERCs for radiation-induced direct reactions in pure H_2O ice show similar magnitudes: 1.2×10^{-2} s^{-1} for X-ray irradiation and 2.5×10^{-2} s^{-1} for Ni ion irradiation, both at low temperatures.

Within the range of irradiation conditions analysed, the highest ERC for direct reactions is observed for Ni ion irradiation of pure CO ice at 13 K, reaching 2.4×10^{-1} s^{-1}. In contrast, the lowest value is found for Ni ion irradiation of pure CO_2 ice at the same temperature, with an ERC of 7.5×10^{-3} s^{-1}. For bimolecular reactions, the highest ERC is associated with $^{16}O^{5+}$ ion irradiation of pure CH_4 ice at 16 K, while the lowest value is recorded for X-ray irradiation of acetonitrile ice at 13 K (9.7×10^{-26} cm^3).

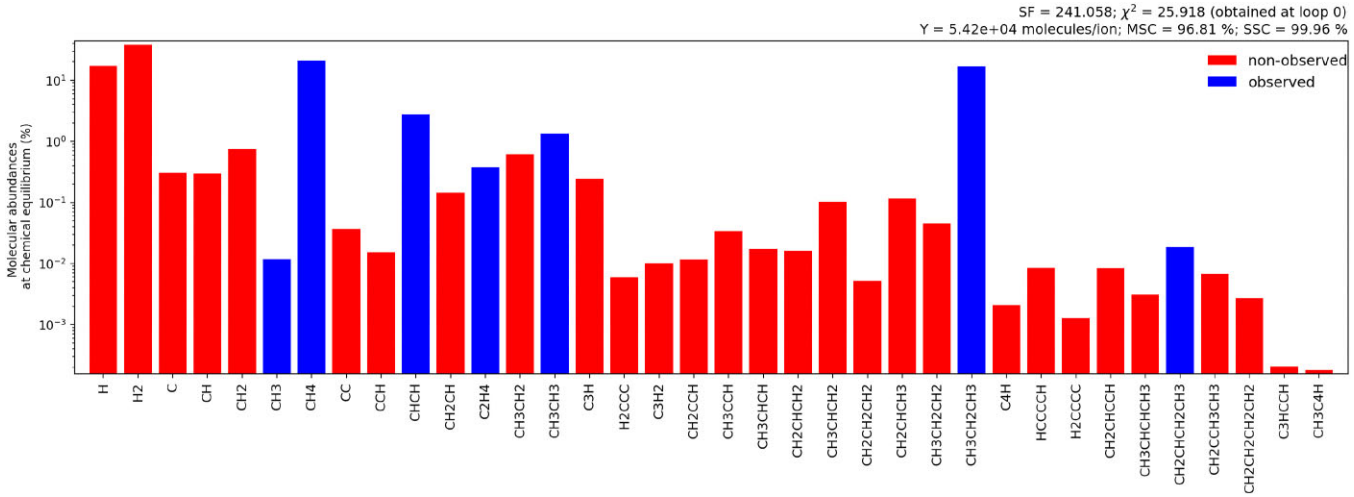

Figure 4. Molecular abundances in percentage at the chemical equilibrium phase (or EBR per cent).

Table 2. List of the molecular abundances of the species in EBR per cent.

Molecular species at the equilibrium chemistry stage	EBR per cent
H	1.7×10^{1}
H_2	3.8×10^{1}
C	3.0×10^{-1}
CH	3.0×10^{-1}
CH_2	7.5×10^{-1}
CH_3	1.2×10^{-2}
CH_4	2.1×10^{1}
CC	3.7×10^{-2}
CCH	1.5×10^{-2}
CHCH	2.8
CH_2CH	1.4×10^{-1}
C_2H_4	3.8×10^{-1}
CH_3CH_2	6.1×10^{-1}
CH_3CH_3	1.3
C_3H	2.4×10^{-1}
H_2CCC	6.0×10^{-3}
C_3H_2	1.0×10^{-2}
CH_2CCH	1.1×10^{-2}
CH_3CCH	3.4×10^{-2}
CH_3CHCH	1.7×10^{-2}
CH_2CHCH_2	1.6×10^{-2}
CH_3CHCH_2	1.0×10^{-1}
$CH_2CH_2CH_2$	5.0×10^{-3}
CH_2CHCH_3	1.2×10^{-1}
$CH_3CH_2CH_2$	4.5×10^{-2}
$CH_3CH_2CH_3$	1.7×10^{1}
C_4H	2.0×10^{-3}
HCCCCH	9.0×10^{-3}
H_2CCCC	1.0×10^{-3}
CH_2CHCCH	8.0×10^{-3}
$CH_3CHCHCH_3$	3.0×10^{-3}
$CH_2CHCH_2CH_3$	1.9×10^{-2}
$CH_2CCH_3CH_3$	7.0×10^{-3}
$CH_2CH_2CH_2CH_2$	3.0×10^{-3}
C_3HCCH	0.0
CH_3C_4H	0.0
Summed EBR	100.0
Summed only observed EBR	42.2
Summed only non-observed EBR	57.8

Table 3 also presents, for comparison purposes, the desorption rates of various species obtained using the current methodology. Among the analysed cases, pure CO_2 ice irradiated by 52 MeV Ni ions exhibited the highest desorption rate, reaching 8.0×10^{4} molecules·ion^{-1}. In contrast, the lowest desorption rate was observed for pure H_2O ice irradiated by X-rays, with a value of 3.7×10^{12} molecules·s^{-1}, approximately two orders of magnitude lower. These differences may be attributed to variations in temperature, activation energies, and the nature of the chemical bonds in each ice sample.

Desorption yields are notably low for ices irradiated with X-rays, with values of 2.6×10^{-2} and 0.23 molecules·photon^{-1} for H_2O and CH_3CN, respectively. Despite this, H_2O still exhibited the highest desorption yield among the X-ray-irradiated ices. The wide range of yield (Y) values reflects a strong dependence on ice composition, radiation type, and temperature. As shown by S. Pilling et al. (2024), higher ice temperatures enhance radiation-induced desorption, leading to increased release of molecules into the gas phase during CR bombardment. This temperature effect was further confirmed by S. Pilling, C. H. Silveira & A. Ojeda-Gonzalez (2023b), who also noted its influence on ERC values.

Future investigations may help clarify the differences in ERCs, desorption rates, and desorption yields among ices of varying composition irradiated by different sources and at different temperatures. As noted by S. Pilling et al. (2023a), current calculations do not account for specific desorption mechanisms or the contribution of excited-state reactive species. Additionally, a key limitation, particularly relevant to CR irradiation, is the lack of distinction between desorbed and sputtered species. It is also recommended that future models consider isotopic exchange between molecules and the diffusion of reactants within the ice bulk.

4 ASTROPHYSICAL IMPLICATIONS

Characterizing chemical reaction mechanisms is crucial for building accurate physical models. In that sense, several methods are available to determine reaction rate coefficients. For instance, quantum chemical computational techniques have shown good agreement with experimental results (I. A. Union & P. D. Singh 1992). One example is the simulation of the ground triplet state of the C_3H_6O molecule,

Table 3. Average ERCs and desorption parameters derived from the best-fitting model for the chemical evolution of CH_4 ice under CR irradiation.

Average Parameter	Pure CH_4 ice at 16 K irradiated by 15.7 MeV $^{16}O^{5+}$ ions (This work)	Pure H_2O ice at 12 K irradiated by X-ray (C. H. da Silveira & S. Pilling 2024)	Pure H_2O ice at 13 K irradiated by 52 MeV Ni ions (C. H. da Silveira & S. Pilling 2024)	Pure CO ice at 13 K irradiated by 50 MeV Ni ions (S. Pilling et al. 2023a)	Pure CO_2 ice at 13 K irradiated by 52 MeV Ni ions (S. Pilling et al. 2022)	CH_3CN ice irradiated by X-rays at 13 K (G. A. Carvalho et al. 2022)
ERC for the intrinsic desorption reactions (k_{ed})	8.3×10^{-5} s^{-1}	1.8×10^{-4} s^{-1}	3.2×10^{-6} s^{-1}	4.4×10^{-4} s^{-1}	2.9×10^{-3} s^{-1}	6.2×10^{-6} s^{-1}
ERC for the radiation-induced direct reactions	3.9×10^{-3} s^{-1}	1.2×10^{-2} s^{-1}	2.5×10^{-2} s^{-1}	2.4×10^{-1} s^{-1}	7.5×10^{-3} s^{-1}	2.3×10^{-3} s^{-1}
ERC for the bimolecular reactions	2.4×10^{-23} cm^3 molecules^{-1}·cm^{-1}	3.9×10^{-25} cm^3 molecules^{-1}·cm^{-1}	4.3×10^{-24} cm^3 molecules^{-1}·cm^{-1}	4.4×10^{-24} cm^3 molecules^{-1}·cm^{-1}	2.4×10^{-25} cm^3 molecules^{-1}·cm^{-1}	9.7×10^{-26} cm^3 molecules^{-1}·cm^{-1}
Desorption rate	2.7×10^{14} molecules·s^{-1}	3.7×10^{12} molecules·s^{-1}	1.7×10^{13} molecules·s^{-1}	7.4×10^{13} molecules· s^{-1}	8.0×10^{14} molecules·s^{-1}	–
Desorption yield (Y)	5.4×10^{4} molecules·ion $^{-1}$	2.6×10^{-2} molecules·photon^{-1}	1.0×10^{4} molecules·ion^{-1}	1.3×10^{5} molecules·ion $^{-1}$	8.0×10^{4} molecules·ion^{-1}	0.23 molecules·photon^{-1}

based on quantum chemical calculations, which was validated using a gas-grain dense cloud model (K. M. Hickson, J.-C. Loison & V. Wakelam 2024). In the present work, we employed the PROCODA code (S. Pilling et al. 2022), as previously described.

Carbon is one of the most abundant elements in the universe, second only to hydrogen. As a result, a wide variety of carbon–hydrogen compounds, including methane (CH_4), are expected to exist in the ISM. Methane has indeed been detected in the atmospheres of several planets and moons within the Solar system, as well as in some exoplanetary atmospheres. However, the detailed chemical pathways leading to methane formation remain poorly understood. The effective reaction rate coefficients obtained in this work provide valuable constraints for future astrochemical models aimed at better understanding these processes.

Our results indicate that methane dissociation predominantly proceeds through the $CH_2 + H_2$ channel, consistent with the findings of (G. A. Carvalho et al. 2022), where CH_4 was formed via chemical reactions following the irradiation of acetonitrile by broad-band soft X-rays. However, these results are not directly applicable to ice mixtures containing oxygen-bearing species, such as H_2O:CH_4 or CO:CH_4. As highlighted by (H. Carrascosa et al. 2020), the intermolecular interactions that bind CH_4 molecules in the ice matrix are highly dependent on the overall composition of the ice mantle. This, in turn, significantly influences both its photodesorption behaviour and photochemical reactivity.

Methane has been identified as a potential precursor in the formation of more complex organic molecules, such as propane (C_3H_8). For instance, Titan's atmosphere; composed primarily of molecular nitrogen and methane (C. A. Nixon 2024); provides a compelling example of conditions favourable to increasing molecular complexity (R. Glaser et al. 2007; S. Pilling et al. 2007, 2009, 2011). Our results also indicate that reactive intermediates such as CH_2, C_3H_6, C_2H_3, C_2H_5, and C_3H, though not yet observed experimentally, may plausibly exist in environments where methane is abundant.

Building on this, it is reasonable to assume that the species highlighted in red in Fig. 4 may indeed be present in astrophysical environments where methane has been detected. Some of these molecules are strong candidates for future observations with advanced telescopes such as ALMA (radio) and *JWST* (IR). For example, diacetylene (HCCCCH) has already been observed in a range of astronomical settings. It was first detected in the dark cloud TMC-1 during a molecular line survey conducted with the Nobeyama 45-m telescope (K. Kawaguchi et al. 1991). In Titan's atmosphere, C_4H_2 is produced in the gas phase at altitudes below 1200 km through reactions involving acetylene and C_2H radicals (B. Fleury, M. S. Gudipati & I. Couturier-Tamburelli 2024).

Further supporting this idea, diacetylene (C_4H_2) has also been observed toward the protostar L1448-mm, where it appears in emission through its ν_8 bending mode at 15.92 μm (M. L. van Gelder et al. 2024). Additionally, high-resolution observations ($R \approx 85\,000$) toward the carbon-rich star IRC+10216, conducted with the TEXES spectrograph on the 3-m IRTF telescope, revealed the presence of two distinct populations of C_4H_2 with rotational temperatures of 420±120 K and 47±7 K, respectively (J. P. Fonfría et al. 2018). Although diacetylene has not yet been detected in very cold environments (10–20 K), it appears clearly in our modelling results. Potential formation pathways for C_4H_2 involve both experimentally observed species like C_2H_2 and others not yet observed, such as atomic C and H, C_4H, C_3H_2, CH, C_3H, CC, and CCH. The capabilities of ALMA in the millimetre and submillimetre regimes make it especially well-suited to search for such complex molecules in molecular clouds

and protoplanetary nebulae. Likewise, *JWST*'s IR sensitivity enables exploration of obscured regions and distant star-forming galaxies where such species might also be found.

The cold pre-stellar core TMC-1, located in Heiles' Cloud 2 in Taurus, is particularly notable for its rich inventory of carbon-bearing molecules (M. Guélin & J. Cernicharo 2022), including nearly saturated species like CH_3CHCH_2, typically associated with warmer star-forming regions (N. Marcelino et al. 2007). Similarly, in the Orion Bar photodissociation region, observations with the IRAM 30 m telescope revealed that nearly 40 per cent of the detected spectral lines originate from hydrocarbons such as C_2H, C_4H, c-C_3H_2, and l-C_3H, among others (S. Cuadrado et al. 2015). More recently, the C_3H^+ cation was detected for the first time in TMC-1, with a column density of $(2.4 \pm 0.2) \times 10^{10}$ cm^{-2} (J. Cernicharo et al. 2022). Other small carbon chains and radicals such as c-C_3H_2 (H. E. Matthews & W. M. Irvine 1985) and the highly abundant propargyl radical (CH_2CCH) (M. Agúndez et al. 2021) have also been identified in this region, reinforcing the idea that cold cores can host considerable molecular complexity, including species also predicted by our simulations.

5 CONCLUSIONS

The main conclusions of this work are summarized as the following:

(i) Using FTIR spectra, a quantitative analysis of the observed species was carried out and used as a basis to infer the presence of species that are not detectable by IR techniques. To support this, a chemical network comprising 1857 reactions among 36 molecular species was developed to simulate the chemical evolution of the ice sample. This modelling approach provides deeper insight into the experimental results by revealing the behaviour and possible abundance of non-observed species.

(ii) The best-fitting models yielded numerical values for the effective reaction rate coefficients. For direct dissociation reactions, the average rate coefficient was $\bar{k}_d = 6.42 \times 10^{-3}$s^{-1}, while the corresponding average dissociation cross-section was $\bar{\sigma}_d = 7.1 \times 10^{-13}$ ions $\cdot$ cm$^{-2} \cdot$ s^{-1}. This cross-section value is more than two orders of magnitude higher than that obtained from CH_4 irradiation with 220 MeV $^{16}O^{7+}$ ions, and about one order of magnitude greater than the value derived from 15.7 MeV $^{16}O^{5+}$ irradiation. Such discrepancies suggest that future models should consider specific desorption mechanisms, including reactive desorption or the involvement of excited-state species. For bimolecular reactions, the average effective reaction rate coefficient was found to be $\bar{k}_{A+B} = 7.02 \times 10^{-25}$ cm$^3 \cdot$ molecule$^{-1} \cdot$ s^{-1}. These average values can serve as inputs in astrochemical models to better track the chemical evolution of ice-phase molecules in environments subjected to CR irradiation.

(iii) The desorption rates and desorption yield were 2.68×10^{14} molecules$\cdot$s^{-1} and 5.42×10^4 molecules$\cdot$ion $^{-1}$, respectively. We also compared these results with others obtained using the same methodology (H_2O, CO, CO_2, and CH_3CN), but irradiated at different temperatures and by different sources. All comparative values of ERC show that the value depends on the composition of the ice, on the temperature and of the radiation source.

(iv) The molecular abundances of both observed and non-observed species at the chemical equilibrium (CE) phase were characterized. The summed EBR of the observed species was only 15.6 per cent lower than that of the non-observed species, indicating that a significant fraction of the chemistry remains hidden from IR detection. All observed species exhibited molecular abundances above 0.012 per cent. Among the non-observed species, H_2 reached a peak abundance of approximately 38 per cent, while CH_4, the most abundant observed species, peaked near 21 per cent. These findings highlight the importance of enhancing observational techniques, particularly to enable the detection of species such as atomic hydrogen and molecular hydrogen, which are crucial components in astrochemical environments but remain inaccessible to conventional IR spectroscopy.

This study provides critical reaction rate coefficients that will enhance future astrochemical models by refining predictions of chemical evolution in interstellar ices under CR irradiation, while also suggesting promising molecular targets for advanced observational campaigns with state-of-the-art telescopes such as ALMA and *JWST*, paving the way for a deeper understanding of organic and prebiotic chemistry in the icy space environments expose to radiation.

ACKNOWLEDGEMENTS

GAC would like to thank CNPq (Conselho Nacional de Desenvolvimento Científico e Tecnológico) for financial support under process #314121/2023-4 and Fundação Araucária for financial support under NAPI 'Fenômenos extremos no Universo'. SG thanks Fundação Araucária for financial support. SP thanks the financial support from the Brazilian agencies CNPq (#302608/2022-2) and FAPESP (Fundação de Amparo à Pesquisa do Estado de São Paulo (#2016/22018-7 and #2024/05115-5).

DATA AVAILABILITY

The data underlying this article are available in the article and in its online supplementary material.

REFERENCES

Aab A. et al., 2017, Science, 357, 1266
Agúndez M., Cabezas C., Tercero B., Marcelino N., Gallego J. D., de Vicente P., Cernicharo J., 2021, A&A, 647, L10
Bell T. J. et al., 2023, Nature, 623, 709
Boduch P. et al., 2015, J. Phys. Conf. Ser., 629, 012008
Boduch Ph., Domaracka A., Fulvio D., Langlinay T., Lv X. Y., Palumbo M. E., Rothard H., Strazzulla G., 2012, A&A, 544, A30
Carrascosa H., Cruz-Díaz G. A., Muñoz Caro G. M., Dartois E., Chen Y.-J., 2020, MNRAS, 493, 821
Carvalho G. A., Pilling S., Galvão B. R. L., 2022, MNRAS, 515, 3760
Carvalho G. A., Pilling S., Gerasimenko S., 2024, MNRAS, 527, 2781
Cernicharo J. et al., 2022, A&A, 657, L16
Cuadrado S., Goicoechea J. R., Pilleri P., Cernicharo J., Fuente A., Joblin C., 2015, A&A, 575, A82
da Silveira C. H., Pilling S., 2024, Adv. Space Res., 73, 1149
de A. Vasconcelos F., Pilling S., Rocha W. R. M., Rothard H., Boduch P., 2017, ApJ, 850, 174
de Barros A. L. F., Bordalo V., Duarte E. S., da Silveira E. F., Domaracka A., Rothard H., Boduch P., 2011, A&A, 531, A160
Dumas C., Merlin F., Barucci M. A., de Bergh C., Hainault O., Guilbert A., Vernazza P., Doressoundiram A., 2007, A&A, 471, 331
Elliot J. L., Strobel D. F., Zhu X., Stansberry J. A., Wasserman L. H., Franz O. G., 2000, Icarus, 143, 425
Faherty J. K. et al., 2024, Nature, 628, 511
Fleury B., Gudipati M. S., Couturier-Tamburelli I., 2024, A&A, 684, A1
Fonfría J. P., Agúndez M., Cernicharo J., Richter M. J., Lacy J. H., 2018, ApJ, 852, 80
Formisano V., Atreya S., Encrenaz T., Ignatiev N., Giuranna M., 2004, Science, 306, 1758

Gaisser T. K., Engel R., Resconi E., 2016, Cosmic Rays and Particle Physics. Cambridge Univ. Press, Cambridge
Gladstone G. R. et al., 2016, Science, 351, aad8866
Glaser R., Hodgen B., Farrelly D., McKee E., 2007, Astrobiology, 7, 455
Glein C. R. et al., 2024, Icarus, 412, 115999
Guélin M., Cernicharo J., 2022, Front. Astron. Space Sci., 9, 787567
Hickson K. M., Loison J.-C., Wakelam V., 2024, ACS Earth Space Chem., 8, 1087
Kawaguchi K. et al., 1991, PASJ, 43, 607
Kim Y. S., Bennett C. J., Chen L.-H., O'Brien K., Kaiser R. I., 2010, ApJ, 711, 744
Kipfer K. A., Galli A., Riedo A., Tulej M., Wurz P., Ligterink N. F. W., 2024, Icarus, 410, 115742
Lacy J. H., Carr J. S., Evans N. J., Baas F., Achtermann J. M., Arens J. F., 1991, ApJ, 376, 556
Linsley J., 1963, Phys. Rev. Lett., 10, 146
Linsley J., Scarsi L., Rossi B., 1961, Phys. Rev. Lett., 6, 485
Lv X. Y. et al., 2012, A&A, 546, A81
Maciel W. J., 2013, Astrophysics of the Interstellar Medium. Springer, New York, https://link.springer.com/book/10.1007/978-1-4614-3767-3
Marcelino N., Cernicharo J., Agúndez M., Roueff E., Gerin M., Martín-Pintado J., Mauersberger R., Thum C., 2007, ApJ, 665, L127
Martín-Doménech R., Manzano-Santamaría J., Caro G. M. M., Cruz-Díaz G. A., Chen Y.-J., Herrero V. J., Tanarro I., 2015, A&A, 584, A14
Matthews H. E., Irvine W. M., 1985, ApJ, 298, L61
Mejía C. F., de Barros A. L. F., Bordalo V., da Silveira E. F., Boduch P., Domaracka A., Rothard H., 2013, MNRAS, 433, 2368
Mifsud D. V. et al., 2023, Atoms, 11, 19
Nixon C. A., 2024, ACS Earth Space Chem., 8, 406
Ohno K., Zhang X., Tazaki R., Okuzumi S., 2021, ApJ, 912, 37
Pilling S., Lago A. F., Coutinho L. H., de Castilho R. B., de Souza G. G. B., de Brito A. N., 2007, Rapid Commun. Mass Spectrom., 21, 3646
Pilling S., Andrade D. P. P., Neto Á. C., Rittner R., Naves de Brito A., 2009, J. Phys. Chem. A, 113, 11161
Pilling S., Duarte E. S., Domaracka A., Rothard H., Boduch P., da Silveira E. F., 2010, A&A, 523, A77
Pilling S. et al., 2011, MNRAS, 411, 2214
Pilling S., Carvalho G. A., Rocha W. R. M., 2022, ApJ, 925, 147
Pilling S., Rocha W. R. M., Carvalho G. A., de Abreu H. A., 2023a, Adv. Space Res., 71, 5466
Pilling S., da Silveira C. H., Ojeda-Gonzalez A., 2023b, MNRAS, 523, 2858
Pilling S., Carvalho G. A., de Abreu H. A., Galvão B. R. L., da Silveira C. H., Mateus M. S., 2023c, ApJ, 952, 17
Pilling S., Mateus M. S., Ojeda-González A., Ferrão L. F. A., Galvão B. R. L., Boduch P., Rothard H., 2024, MNRAS, 528, 6075
Poro A., Farahani F. A., Bahraminasr M., Hadizadeh M., Kodini F. N., Rezaee M., Gargari M. S., 2021, A&A, 653, L7
Sicardy B. et al., 2024, A&A, 682, L24
Union I. A., Singh P. D., 1992, Astrochemistry of Cosmic Phenomena. Kluwer, Dordrecht, https://www.amazon.com.br/Astrochemistry-Cosmic-Phenomena-P-D-Singh/dp/0792318242
van Gelder M. L. et al., 2024, A&A, 692, A197
Vasconcelos F. A., Pilling S., Rocha W. R. M., Rothard H., Boduch P., Ding J. J., 2017, Phys. Chem. Chem. Phys., 19, 12845
Vasconcelos F. A., Pilling S., Agnihotri A., Rothard H., Boduch P., 2020, Icarus, 351, 113944
Williams J. P., 2021, Introduction to the Interstellar Medium. Cambridge Univ. Press, Cambridge

SUPPORTING INFORMATION

Supplementary data are available at *MNRAS* online.

chem_reactions.txt
k_values.csv

Please note: Oxford University Press is not responsible for the content or functionality of any supporting materials supplied by the authors. Any queries (other than missing material) should be directed to the corresponding author for the article.

This paper has been typeset from a TEX/LATEX file prepared by the author.